Geomorphology 423 (2023) 108560

Contents lists available at ScienceDirect

Geomorphology

journal homepage: www.journals.elsevier.com/geomorphology

Assessing probability of failure of urban landslides through rapid characterization of soil properties and vegetation distribution

Sylvain Fiolleau *, Sebastian Uhlemann, Nicola Falco, Baptiste Dafflon

Lawrence Berkeley National Laboratory, Earth and Environmental Sciences Area, Berkeley, CA, USA

ARTICLE INFO

Keywords:
Landslide Risk
Probability of failure
Geophysics
Remote Sensing

ABSTRACT

Landslides are a major natural hazard, threatening communities and infrastructure worldwide. The mitigation of these hazards relies on the understanding of their causes and triggering processes, which depends directly on soil properties, land use, and their changes over time. In this study, we propose a novel framework to estimate the probability of failure in highly developed urban areas. The framework combines remote sensing and geophysical data to estimate soil properties and land covers. Such estimate properties are then integrated into a hydro-geomechanical model to provide a robust estimate of the probability of failure. To assess the importance and sensitivity of the input parameters to the probability of failure assessment, a sensitivity analysis was performed on the seven main parameters (density, friction angle, cohesion, soil thickness, slope, water recharge and saturated hydraulic conductivity) of the hydro-geomechanical model. Slope angle, soil thickness and cohesion are shown to be the most important parameters. While the slope angle can be derived from high-resolution digital elevation models, soil thickness and cohesion cannot be assessed. To incorporate the variability of these two parameters into the model, seismic noise measurements were performed to estimate soil thickness. Supervised classification of remote sensing data was used to map vegetation type and related root cohesion, which can impact the cohesion significantly. The results show that slopes with relatively thick soil layers (above 2 m) have up to four times higher probability of failure. Slopes with tall vegetation cover, and hence comparably high root cohesion, reduce the probability of failure, particularly when the soil layer is relatively thin (< 3 m). The developed approach makes use of rapid to acquire geophysical and easily to obtain remote sensing data, and hence is transferable to other study sites. This approach may be of particular importance to areas of active vegetation management that may cause considerable changes in landslide hazard maps.

1. Introduction

Landslides are a major natural hazard endangering communities and infrastructures worldwide, causing a considerable number of casualties and economic losses in the last decade (Froude and Petley, 2018). Haque et al. (2019) show that in 20 years (1995–2014) landslides caused a total of 163,658 deaths worldwide. According to the USGS, in the United States, landslides cause an estimate of more than $1 billion in damages and about 25 to 50 deaths each year. Climate change is resulting in shifting precipitation pattern, with increasing frequency of extreme storm events, and is leading to an increasing number of shallow landslides (Patton et al., 2019; Coe, 2020; Lin et al., 2020). Hence, it is important to mitigate the risk posed by landslides, and a crucial part of that is a thorough assessment of the landslide hazard (Corominas et al., 2013). Urban areas, which usually have high exposure and high vulnerability (the other factors defining the landslide risk), often show very high landslide risk in case of high landslide susceptibility. Hence, providing an accurate estimated of the landslide hazards, e.g. in terms of probability of failure (PoF), is critical to assessing the risk (Cheung, 2021).

The landslide susceptibility can be quantified through different approaches, depending on prior knowledge and the scale of the studied area. The three main approaches can be classified as heuristic, statistical, or deterministic (Guzzetti et al., 1999; Regmi et al., 2014). The heuristic method, frequently used during the 70's and 80's (Aleotti and Chowdhury, 1999), involves geomorphological mapping of type and degree of the hazard based on expert knowledge. A major drawback of this method is the subjectivity in selecting data and factors governing slope stability. Statistical methods are a commonly used approach applied to large or inaccessible areas, and are based on multivariate and bivariate

* Corresponding author.
E-mail address: sfiolleau@lbl.gov (S. Fiolleau).

https://doi.org/10.1016/j.geomorph.2022.108560
Received 30 May 2022; Received in revised form 12 December 2022; Accepted 14 December 2022
Available online 21 December 2022

statistical techniques (Reichenbach et al., 2018; Kalantar et al., 2020), linking geological and geomorphological information with former landslide distributions. Among the most commonly used are logistic regression (Akgun, 2012; Devkota et al., 2013; Park et al., 2013; Chen et al., 2016), artificial neural networks (Yilmaz, 2010a; Nourani et al., 2014; Tsangaratos and Benardos, 2014; Gorsevski et al., 2016; Tien Bui et al., 2016; Li et al., 2021), support vector machines (Yilmaz, 2010b; Marjanović et al., 2011; Tien Bui et al., 2016), and random forest methods (Youssef et al., 2016; Chen et al., 2017). These approaches commonly involve a sensitivity analyses on predisposing parameters in order to improve the predictive capability of models (Chen et al., 2018; Di Napoli et al., 2021). Deterministic methods are generally based on the calculation of the factor of safety (Regmi et al., 2014), which is the ratio of restraining to driving forces, and hence requires a numerical calculation of the forces acting onto a slope. These can be calculated using fixed, i.e. static, or temporally varying, i.e. dynamic, boundary conditions. These methods require quantitative information such as hydrological information (soil saturation, permeability, hydraulic conductivity, etc.) and geotechnical information (soil thickness, cohesion, internal friction angle, density, etc.) (Montrasio et al., 2011; Jovančević et al., 2013; Palazzolo et al., 2021). Deterministic methods are considered more accurate than heuristic and statistical methods because physical processes are integrated and quantitative stability values are computed (Corominas et al., 2013). However, considering the large amount of a priori knowledge required, the application of those methods has been limited to local to regional scales (Cervi et al., 2010; Zizioli et al., 2013).

Deterministic approaches use physical models to calculate the stresses in the slope based on various governing equations and discretization methods. Hence, understanding the sensitivity of the input parameters on the results of a certain model is crucial to understanding the uncertainty of the results. Studies have shown that among the parameters required for slope stability analysis, the slope angle and soil thickness are often the most sensitives (van Westen et al., 2006; Segoni et al., 2012; Choo et al., 2019; Min and Yoon, 2021). The sensitivity to other parameters can be more site-specific. For example, Choo et al. (2019) performed a sensitivity analysis on the slope stability calculations of Mt. Geohwa in South Korea and showed that while the slope angle and soil thickness strongly influence the factor of safety, also the friction angle had a strong impact on the slope stability estimation. The cohesion and density of the soil showed only minor impact. However, the type of model and the characteristics of the study area determine which parameters have the strongest control on the slope stability estimates. Hence, it is necessary to perform a sensitivity study to understand the uncertainties of the landslide hazard assessment of an area, and to determine which parameters have to be known most accurately to obtain reliable results.

Vegetation has been recognized to play an important role on the stability of slopes (Band et al., 2012; Hwang et al., 2015; Sidle and Bogaard, 2016; Cohen and Schwarz, 2017; Phillips et al., 2021). By adding weight to the slope, it can increase the load and thus reduce the stability, increasing the failure probability. However, in the case of a shallow landslide, this effect is largely compensated for by the increase in cohesion that is added by the root network and by the reduction in moisture content (and hence in pore water pressure), thus increasing the factor of safety (Forbes and Broadhead, 2013). Among these factors, decreasing cohesion is known to have the largest influence on slope instability (Sidle and Ochiai, 2006; Sidle and Bogaard, 2016). To account for this in slope stability modelling, a simple approach is to consider a total cohesion and to directly add the cohesion induced by the presence of the root network to the soil cohesion (Mattia et al., 2005; Ji et al., 2012; Kim et al., 2017; Emadi-Tafti et al., 2021).

An important issue with the vegetation cover is that it varies over space and time (e.g. due to land management or wildfire). Wildfire constitutes one of the main cause of vegetation destruction and plays a major role in landslide triggering (De Graff, 2018; Rengers et al., 2020). Numerous studies have shown that root cohesion can be drastically reduced following fire, leading to slopes being more prone to failure (Jackson and Roering, 2009; Lanini et al., 2009; Gehring et al., 2019).

The spatial and temporal uncertainty of the model parameters is one of the major challenges in assessing the landslide hazard (Sidle and Ochiai, 2006; van Westen et al., 2006; Anagnostopoulos et al., 2015). To address this uncertainty, probabilistic approaches are often used (Hammond et al., 1992; Nilsen, 2000; Strauch et al., 2018; Lee et al., 2020). Strauch et al. (2018) developed a regional model of probabilistic slope failures and applied it to the North Cascades National Park Complex in the state of Washington, USA. They used a Monte Carlo simulation, facilitated by the python package *Landlab* (Hobley et al., 2017), allowing them to incorporate the uncertainty in model parameters. Their study highlighted the high influence of soil thickness on the landslide prediction, as well as the stabilizing effect of tall vegetation.

The aim of this study is to investigate the value of including detailed spatial distributions of soil thickness and vegetation into slope stability estimates, as these spatially (and temporally) varying inputs strongly affect the landslide hazard assessment, particularly for shallow landslides, Recent development in geophysical and remote sensing methods have allowed for a relatively quick estimation of those parameters across large domains, and, in the case of the vegetation distribution, over time. Hence, we propose a novel approach, combining geophysical and remote sensing data to account for the spatial variability of the most important input parameters (slope angle, soil thickness and cohesion) for the PoF calculation. The soil thickness is estimated based on seismic ambient noise measurements and the computation of the H/V (Horizontal to Vertical) ratios, which have been shown to provide reliable estimates of the thickness of unconsolidated material above bedrock (Guéguen et al., 2007; Méric et al., 2007; Bièvre et al., 2011; Yılmaz et al., 2021). To retrieve the vegetation cover and its changes over time across the study site, we used satellite images of two periods encompassing a tree removal for wildfire hazard mitigation and perform land cover classification. By comparing the resulting PoF maps, we evaluate the influence of the model input parameters on the slope stability assessment and the need to include detailed spatial estimates of soil thickness and vegetation distribution.

2. Study site

The study site is located in the densely populated San Francisco Bay Area on the western flank of the northwest-trending Berkeley Hills (Fig. 1), and comprises the Lawrence Berkeley National Laboratory, which houses many nation-critical research facilities. The seismically-active San Francisco Bay area includes a series of major northwest-trending active faults. The closest of these is the Hayward Fault, which lies near the base of the hills. The Hayward fault is among the fault systems with the highest probability of generating a large-magnitude earthquake within the next 30 years (Field, 2008).

The site exhibits a significant landslide hazard due to its geologic and geomorphological history. The bedrock geology is complex in this part of the Berkeley Hills, comprising a variety of moderately to highly deformed sedimentary, volcanic, and metamorphic rock units. The oldest formation corresponds to the Great Valley Complex (Jurassic-Cretaceous, 159–99 Ma) originally deposited in a marine environment, which is locally overlain by sedimentary and volcanic rocks of Tertiary age. The Orinda Formation (13.5–10.5 Ma) is described as distinctly to indistinctly bedded siltstone, claystone, sandstone, and conglomerate. The conglomerates were deposited under alluvial fan conditions, while the sandstone, claystone and finer-grained conglomerates were deposited as flood plain and channel materials (Jones and Curtis, 1991). The Miocene Moraga Formation (10.2–9 Ma) is of volcanic origin consisting of andesite and basalt flows (Wahrhaftig and Sloan, 1989). During the late Miocene and early Pliocene (11.2 to 3.6 Ma), an extended period of compression occurred, resulting in folding, faulting, and uplift of the Berkeley Hills. These processes weakened the formations in place at that

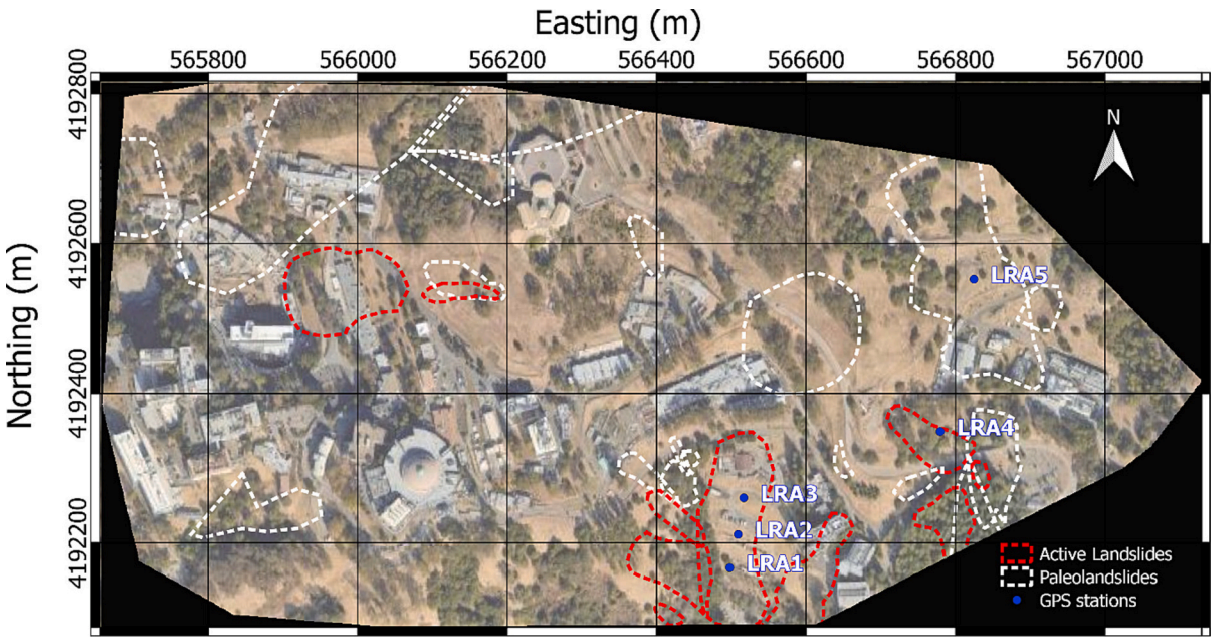

Fig. 1. Study site map showing GNSS station (LRA1 to 5) locations, and the footprint of paleo- and the active landslides.

time (i.e., highly fracture and weathered siltstone and claystone with a silty to fine gravelly matrix), which are now subject to landsliding and erosion. These formations outcrop or are covered by a thin layer of colluvium or fill material, mainly composed of clayey soils with moderate to high expansion potential. Near the base of the hills, Quaternary-age colluvium and landslide deposits (up to 30 m thick) locally overlie bedrock and alluvial deposits (Kropp Alan and Associates, 2006).

The study site has a long history of landsliding with the presence of large paleolandslides (Fig. 1), and numerous recent and active failures. A network of five GNSS (Global navigation satellite system) stations has been installed in 2012 and is monitoring three of those (Cohen-Waeber, 2018, Fig. 1). One of these landslide areas (LRA4), which is impacting a bridge critical for emergency response of the Berkeley Hills, is also being monitored using various geophysical and environmental sensors since 2019 (Uhlemann et al., 2021). This landslide can be described as a slow-moving clay rotational slide (Hungr et al., 2014), which takes place in the clayey deposit corresponding to paleolandslide deposits overlying the Orinda Formation (Kropp Alan and Associates, 2006), which are only a few meters thick. Grasses cover most of the site, while the tall vegetation cover comprises mostly *eucalyptus globulus*, but also *pinus radiata* and occasional *coast live oak*.

3. Model and data inputs

3.1. Probability of failure (PoF)

Hazard assessment of the study area was performed by computing the PoF over a year. We used the Landslide Probability component of Landlab (Strauch et al., 2018), which is based on the common infinite slope stability model to compute the factor of safety:

$$FS = \frac{(C_s + C_r)/h_s\rho_s g}{sin\theta} + \frac{cos\theta tan\varnothing(1 - R_w\rho_w/\rho_s)}{sin\theta}, \quad (1)$$

where C_s correspond to the soil cohesion (Pa), C_r is the root induced cohesion (Pa), h_s is the soil depth perpendicular to the slope (m), ρ_s and ρ_w correspond to the saturated bulk density and water density (kg.m^{-3}), respectively, g is the acceleration due to gravity (m.s^{-2}), θ is the slope angle (°), and $\varnothing$ the soil internal friction angle (°). The relative wetness R_w, which corresponds to the ratio of the subsurface flow depth and the soil thickness, is defined as:

$$R_w = min\left(\frac{R\,a}{Tsinsin\,\theta}, 1\right), \quad (2)$$

with R the uniform rate of recharge (md^{-1}) across the upslope specific contributing area a (m), and T the local soil transmissivity (m^{2}d^{-1}). Eq. (1) was solved using a Monte Carlo method with 1000 iterations, based on a priori distributions of the ground water recharge varying over one year and the cohesion distribution. This allows us to consider the time variability and the uncertainty of these input parameters.

Finally, the annual Probability of Failure, *PoF* at each model grid cell was calculated following

$$PoF = PoF(FS \leq 1) = \frac{n(FS \leq 1)}{N} \quad (3)$$

With n the number of iterations which met the failure criterion ($FS \leq 1$) and N the number of iterations.

This approach was preferred to others such as TRIGRS (Baum et al., 2008), since it is developed to provide an annual PoF based on a distribution of hydro-meteorological events (rather than single rainstorm events) and is readily setup to account for uncertainty in the critical input parameters (such as friction angle, water recharge, soil cohesion, etc.). Previous studies have obtained promising results using this method (Strauch et al., 2019).

3.2. Sensitivity analysis

To estimate the importance of each input parameter, a sensitivity study was performed by calculating the Sobol indices using UQLab (Marelli and Sudret, 2014). The Sobol method, also called Analysis of Variance (ANOVA), describes the total variance of the model in terms of the sum of the variances of the inputs (Sobol'', 2001). This approach allows us to determine the influence of each input on the model outcome, by excluding the interaction with other parameters, and only considering the first order indices.

3.3. Root cohesion calculation

As shown in the FS calculation (Eq. (1)), the cohesion term is defined as the sum of soil and root cohesion. The root cohesion was calculated

following the simple perpendicular root model (Waldron, 1977; Wu et al., 1979) which defines the root induced cohesion (C_r) as:

$$C_r = Tr\,(sin\theta + cos\theta\, tan\varnothing)\left(\frac{Ar}{A}\right) \quad (4)$$

Tr is the average tensile strength of roots per unit area, $\frac{Ar}{A}$ (unit less) is the root area ratio (RAR), ∅is the angle of internal friction of the soil, and θ is the angle of deformed roots with respect to the shear surface. Based on an extensive sensitivity analysis, the value of ($sin\theta + cos\theta\ tan\varnothing$) is often approximated to be 1.2 (Wu et al., 1979). However, it tends to overestimate the cohesion, hence, this value has been replaced by the factor $k" = 0.48$, which is an empirical correction factor introduced by Preti (2006) to reduce the overestimated cohesion values, giving:

$$Cr = 0.48{*}Tr\left(\frac{Ar}{A}\right) \quad (5)$$

This corrected $C_r$has been applied to various type of sites (Ji et al., 2012; Mao et al., 2014; Liu et al., 2021) and has been shown to provide results that are comparable to those obtained using more complex fiber bundle models (FBMs) (Mao et al., 2014). Although, more advances models such as energy-based FBM (Ji et al., 2020) may result in more accurate C_r, they require considerably more input parameters, such as the modulus of elasticity of roots and the root distribution, which are difficult to obtain.

Root cohesion estimation was performed by considering the dominant tress species at the study site: *pinus radiata*, *coast live oak*, and *eucalyptus globulus*. The RAR was calculated at 10 cm depth intervals for *eucalyptus globulus* and *pinus radiata* species based on (Sudmeyer et al., 2004), and based on (Canadell et al., 1996) for *coast live oak* species. Root tensile strength information were taken from Kuriakose and van Beek (2011) for *eucalyptus globulus* and *pinus radiata* species, and from Norris (2005) for *coast live oak* species. This gave a root cohesion values at 10 cm depth intervals to the maximum root depth for each species (13, 2, and 10.7 m for *eucalyptus globulus, pinus radiata*, and *coast live oak*, respectively). For each depth, the minimum, modal and maximum root cohesion, were computed as a function of the dominant tree species.

Finally, for each pixel classified as tall vegetation, the minimum, modal and maximum root cohesion (C_r) for the depth corresponding to the soil thickness, was added to the minimum, modal, and maximum soil cohesion (C_s), respectively.

3.4. Model inputs

The slope angle was computed from a digital elevation model with a 1 m resolution derived from a 2018–2019 USGS LiDAR dataset, obtained through the NOAA. The data set has a reported vertical accuracy of 0.087 m, with an average point density of the underlying LiDAR data of 2.78 pts./m^2 (Quantum Spatial, 2019).

Soil parameters were derived from previous geotechnical campaigns (Kropp Alan and Associates, 2006). The soil transmissivity, density, and friction angle were set to 0.001 m^2/day, 1885 kg/m^3, and 24°, respectively. Soil cohesion was represented using a distribution with a minimum, maximum, and modal cohesion of 5 kPa, 15 kPa, and 7.75 kPa, respectively.

3.5. Soil thickness

Soil thickness was mapped from previous geotechnical investigations and seismic ambient noise measurements (A3GEO, Inc., 2020). Previous active seismic campaigns showed that there is a high impedance contrast between the bedrock and the soil layer. While the bedrock shows an average S-wave velocity of 750 m/s ± 90 m/s, the soil layer is characterized by an average of 250 m/s ± 50 m/s (A3GEO, Inc., 2020). In such cases, using the horizontal to vertical spectral ratio technique (H/V technique) applied to ambient seismic noise recordings, has been proven to be a robust and rapid exploration tool for mapping soil thickness (Guéguen et al., 2007; Le Roux et al., 2010). Measurements were performed with a three-component 4.5 Hz sensor at 31 locations. Seismic noise was recorded during 3 h at a sampling frequency of 200 Hz. Data were processed with the Sesarray package (Wathelet et al., 2004). Microtremor records were cut into 10 s time windows, for which Fourier spectra were computed and smoothed using the technique proposed by (Konno and Ohmachi, 1998). For each location, the H/V spectral ratios were computed for all time windows, and the mean H/V curve and its standard deviation was determined. For each point, the resonance frequency (F_0, Hz) was extracted from the H/V peak exhibiting an amplitude >3 (SESAME, 2004). The soil depth (h, m) was inferred from the resonance frequency and the mean S-wave velocity (Vs, 250 m/s) using $h = Vs/4F_0$ (Kramer, 1996).

3.6. Vegetation classification

Vegetation is an important agent in stabilizing steep slopes notably by increasing the soil cohesion (Phillips et al., 2021). However, manual assessment of the distribution of vegetation cover can be time-consuming and difficult to perform on complex terrain. Furthermore, vegetation cover changes over time due to natural processes, but also land management practices, or disturbances, such as wildfire (Rengers et al., 2020). Considering those frequent changes and the time needed to manually map the vegetation distribution, we used satellite image classification to rapidly extract vegetation cover. To assess changes in the landslide hazard due to vegetation management purposes, here we focus on two periods, between which vegetation was cleared at a specific area of the study site. This clearance was done as part of a wildfire fuel clearance effort in April 2021.

The vegetation land-cover analysis over the two periods (before and after tree removal) was assessed by performing image classification four PlanetScope ortho-images acquired on October 26, 2020 and January 9, 2021 for the first period, and on April 18 and June 29, 2021 for the second one. Each image was composed of 4 spectral bands (red, green, blue, and near infrared) with a resolution of 3 m per pixel. Due to the relatively small size of the study area, the selection of training and testing samples and the classification were performed on 1647 × 1670 pixel images (4941 × 5010 m) that extends beyond the study area. A common training and testing data set was used for both periods. Prior to classification, the two tiles of each periods were merged into a final raster composed of 8 bands (2 acquisitions of 4 bands for each period) using QGIS (2020).

The objective of the land-cover analysis was to classify the image into 4 distinct classes: Tall vegetation corresponding to tree coverage, low vegetation corresponding to shrubs, bare soil corresponding to grass or bare soil depending on the season, and others corresponding mainly to build environment.

A supervised classification was conducted using the sklearn python toolbox (Pedregosa et al., 2011). 100-point samples were selected for each class. These samples were split into 80 for training and 20 for testing. Two of the most widely used supervised algorithms were tested, random forest (RF, Erinjery et al., 2018; Liu et al., 2018) and support vector machines (SVM, Falco et al., 2021, 2020; Mountrakis et al., 2011). For the RF, hyper parameters including the maximum depth of the tree and the number of trees in the forest (n_estimators), were tuned by cross-validation in a search space with the following parameter ranges: max_depth = {1,2, …,20} and n_estimators = {1, 2, …, 300}. The cross-validation determined the best parameters for high classification accuracy to be a maximum depth of 12 and 9 corresponding to a number of trees of 21 and 40 for the first and second period, respectively. For the SVM, hyper parameters including the kernel (k), the regularization parameter (C), and the gamma parameter (γ), were tuned by cross-validation in a search space with the following settings: k = {'rbf', 'polynomial'}, C = {0.01, 0.1, …, 10,000} and $\gamma = \{1 \times 10^{-9}, 1 \times 10^{-8}, 1 \times 10^{-7}, \ldots, 1000\}$. The C defines the tolerance of the model to

allow for misclassification of data points. The γ defines how far the influence of a single training example reaches. The cross-validation determined the best parameters for high classification accuracy to be a radial basis function (RBF) kernel with $C = 100$, $\gamma = 1 \times 10^{-7}$ and $C = 10$, $\gamma = 1 \times 10^{-6}$ for the first and second period, respectively.

4. Results

4.1. Sensitivity analysis

Fig. 2 shows the first-order Sobol indices for each parameter and its confidence interval for the 0:025 and 0:975 quantiles. The results of this sensitivity study indicate that slope angle, soil thickness, and cohesion ($C_r + C_s$) have the strongest impact on the estimated PoF, while the influence of soil density, friction angle, transmissivity, and water recharge are at least on order of magnitude smaller. This confirms that slope angle, soil thickness, and the soil cohesion are the most critical parameters when evaluating the PoF using this probabilistic approach, and hence their distribution has to be known most precisely.

4.2. Soil Thickness variations

The soil thickness was mapped from geotechnical and H/V measurements (42 boreholes, 31 ambient noise recordings, Fig. 3) using an inverse-distance-weighted (IDW) interpolation. Fig. 3b shows two H/V analyses, one representative for a deep and one for a shallow bedrock. HV-1 shows a peak with an amplitude of 3.5 at 4 Hz, which leads to 15.6 m bedrock depth estimate. HV-2 shows a peak with an amplitude of about 7 at 35 Hz, estimating the bedrock to be at 1.8 m depth.

The uncertainty of the thickness map is related to bedrock depths values (Boreholes and H/V), the point density and the interpolation. For the bedrock depth values, the uncertainty is estimated to be a few centimeters for borehole records, and for H/V it is directly related to the uncertainty on Vs, which ranges from 200 to 300 m/s in our study case. This leads to an uncertainty of 0.15 m for very thin soils, up to 3 m for the thickest areas (18 m) and ± 0.65 m for the average thickness (3.25 m).

The soil layer is relatively thin over the study area with an average thickness of 3.25 m. The thickest soils can be found in the north-eastern part of the study area of about 18 m thickness, whereas bedrock outcrops (soil thickness of 0 m) are found in the eastern and central. The thick soil cover of the north-eastern part is related to comparably less excavations due the presence of fewer buildings. Fig. 3c shows the variation of soil thickness with slope angle, and shows that the mean thickness of about 3.25 m is present across almost all slope angles, except for flat surfaces where the mean thickness decreases to 2 m. However, the standard deviation shows considerable variability, highlighting the presence of a larger range of soil thickness for slopes ranging from 10° to 25°.

4.3. Vegetation variation

Two vegetation classification algorithms were tested to calculate the PoF incorporating the root cohesion The RF classification classified the 5x5km area with an overall accuracy of 86 % and 89.25 % for the first and second period, respectively, while the SVM algorithm classified it with an overall accuracy of 93.6 % and 91.4 %, respectively. Considering those results, the SVM classification was used to extract the tall vegetation of the study area.

Fig. 4 shows the result of the classification of the vegetation cover for the second period over the study area. Globally, all trees are classified as low or tall vegetation except for rare isolated trees, which seem misclassified as bare soil. The vegetation (low and tall) represents about one third of the study area (Fig. 4).

4.4. PoFs

The influence of integrating the spatial variability of soil thickness and root cohesion in the PoF calculation is assessed through estimating the PoF in three different ways, (1) accounting only for slope angle (PoF_S), (2) including soil thickness (PoF_ST) and (3) including root cohesion (PoF_STV) based on the vegetation cover classification of the second period (April–June 2021).

To assess only the impact of the slope angle (PoF_S, Fig. 5a), the soil thickness was set to a constant value of $h_s = 3.25$ m (corresponding to the mean soil thickness over the study area). No root cohesion was added to the soil cohesion distribution with a minimum, modal and maximum value of 5 kPa, 15 kPa, and 7.75 kPa, respectively. The other parameters were set as described in Section 2. Fig. 5b shows the distribution of slopes over the study area, highlighting numerous slopes >40°, and up to 60° for some localized areas. The slope distribution and the PoF map are correlated, showing high probability (>0.75, red areas) for slopes above 40°. The mean PoF_S over the whole study area is 0.26. Considering its spatial distribution, Fig. 5a shows a high PoF on unbuilt areas, while flat areas (mostly covered by buildings) show a negligible PoF.

Including the soil thickness estimates in the PoF calculation, allows us to consider 2D variations of both the slope angle and soil thickness (PoF_ST, Fig. 5c). Fig. 5c shows that the high PoFs (close to 1) are located in areas of thick soil cover (above 4 m, particularly in the north-eastern

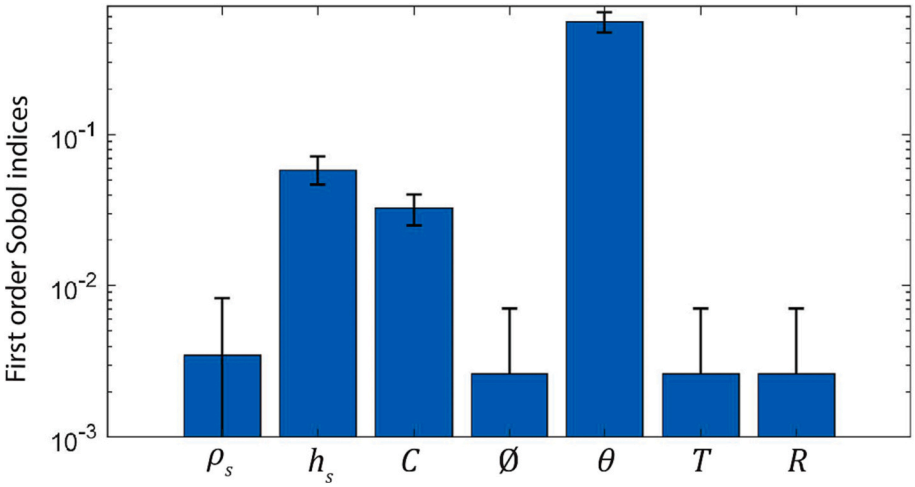

Fig. 2. First Sobol indices of the 7 parameters (soil density ρ_S, soil thickness h_S, cohesion ($C = C_r + C_s$), friction angle ∅, slope angle θ, transmissivity T and water recharge (amount and shape) R used to calculate the factor of safety and its confidence interval.

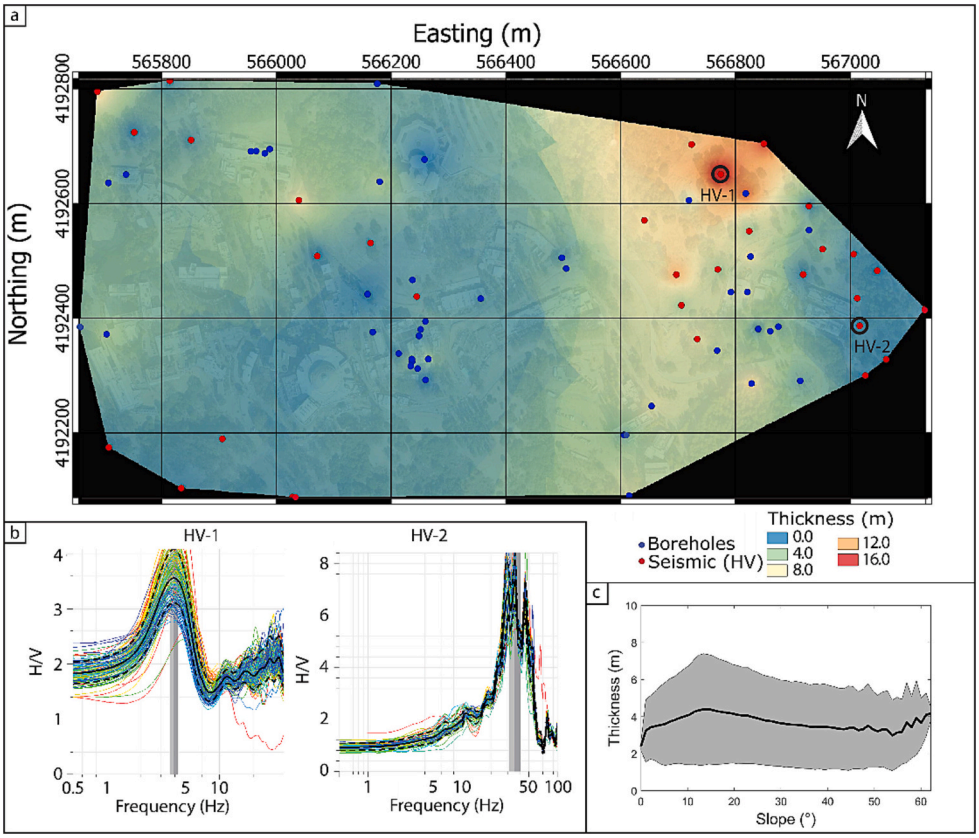

Fig. 3. a) Soil thickness map interpolation from geotechnical (boreholes, blue points) and seismic data (HV measurements, red points). Google satellite background map. b) Examples of H/V curves in the thickest part of the soil (HV-1) and in a thin soil layer (HV-2). c) Mean thickness distribution and its standard deviation as a function of slope angle.

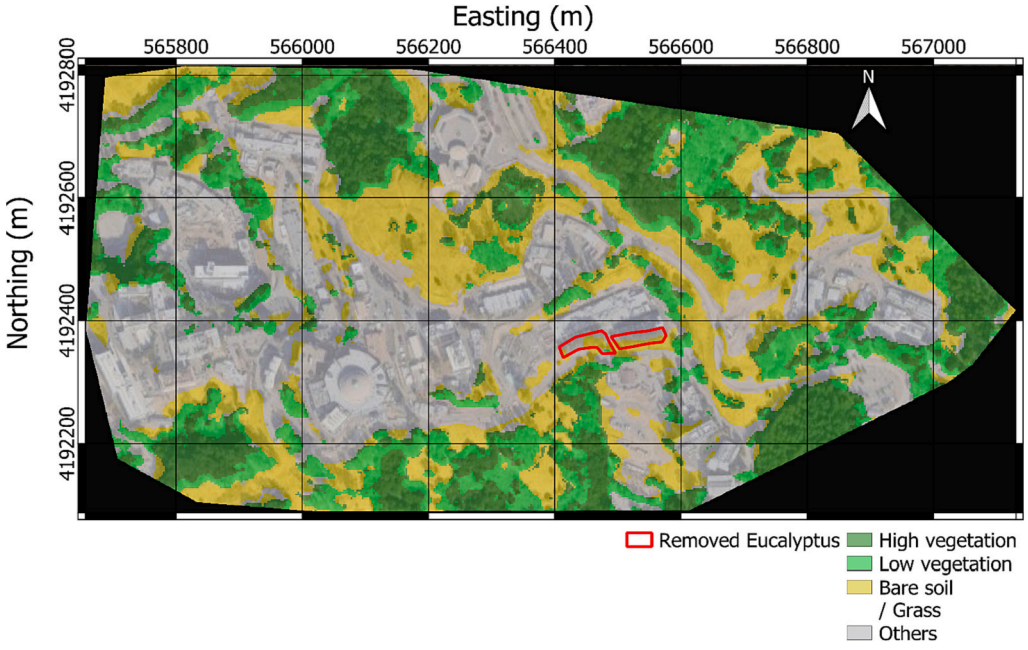

Fig. 4. Result of the SVM classification of the second period (April–June 2021): tall vegetation, low vegetation, bare soil, and others over the study area.

part), while lower PoF (< 0.5) are found in the central and south-western parts. The difference between PoF_ST and PoF (Fig. 5d) shows values increasing by up to 0.75 and values decreasing by as much as −1. The change in the PoF was calculated from the average soil thickness of 3.25 m, corresponding to the boundary between the positive and negative impact of soil thickness variation (gray, Fig. 5d). A decrease was observed for all areas exhibiting soil thickness below 3.25 m. Particularly in the central, eastern, and southern part of the study area,

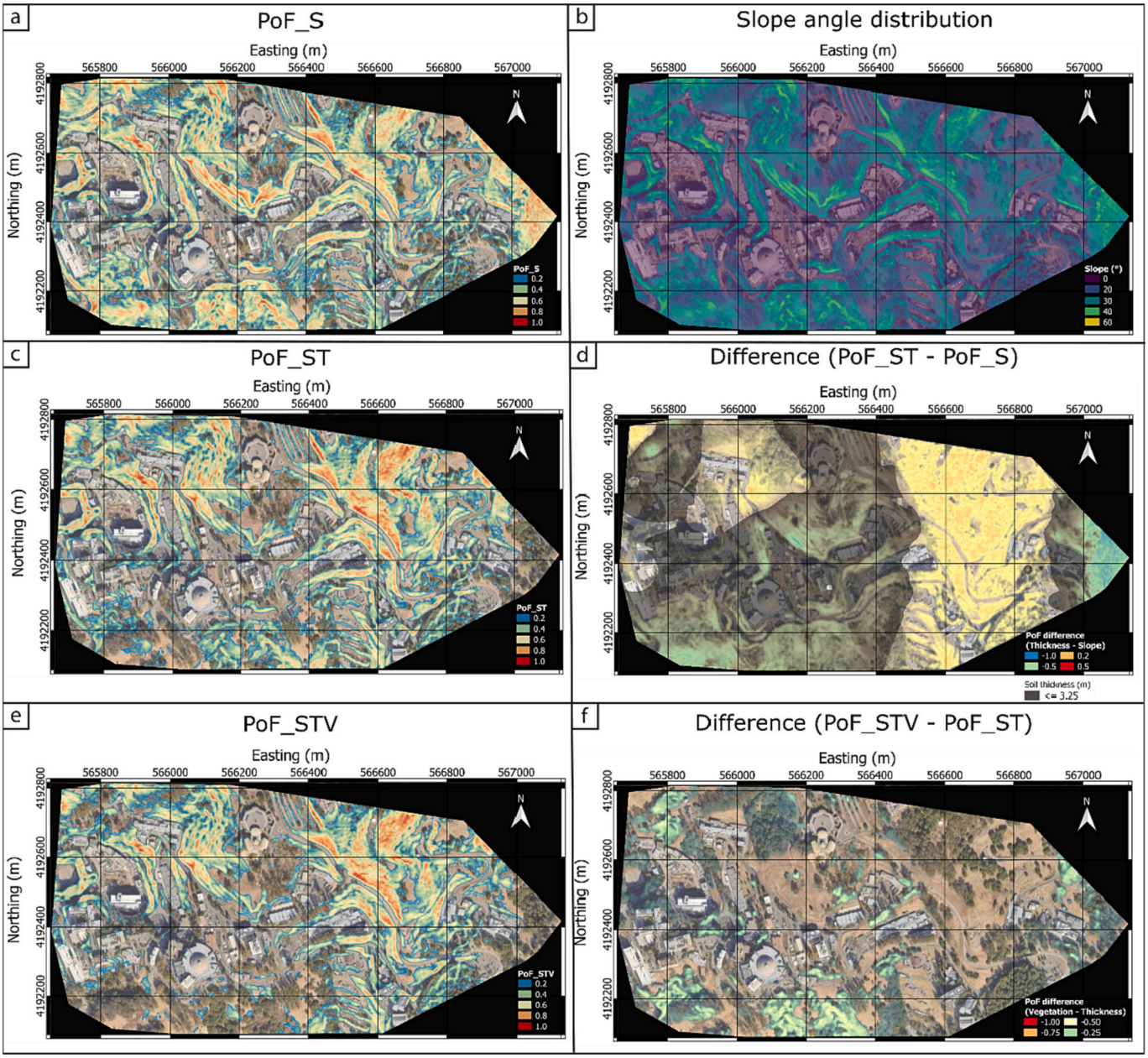

Fig. 5. a) PoF map considering only slope variations (PoF_S). b) Slope distribution c) PoF map considering slope and soil thickness variations (PoF_ST). d) PoF_ST – PoF_S. e) PoF map considering slope, soil thickness and root cohesion variations (PoF_STV). f) PoF_STV – PoF_ST.

the PoF_ST decreases from 1 to 0 due to a soil thickness below 1 m. On the contrary, PoF_ST increases for areas with soils thicker than average soil layer, particularly in the northeastern part of the study area. On average, the PoF decreases from 0.26 to 0.22 when considering a variable soil thickness across the study area.

Fig. 5e shows the probability of failure considering all the important variables: slope angle, soil thickness, and varying root cohesion due to the distribution of tall vegetation (PoF_STV). Considering also the additional root cohesion leads to a further decrease in the average PoF to 0.19. Analyzing the differences between the two probability maps (PoF_STV-PoF_ST, Fig. 5f) shows that the strongest decreases (up to −0.9) in PoF are linked to tall vegetation cover on thin soils, corresponding mostly to the southern and southwestern parts.

Fig. 6a shows the mean PoFs (PoF_S, PoF_ST and PoF_STV) and associated standard deviations as function of slope angle. The PoF_S is zero for slope angles below 18° (Fig. 6a, black) and increases linearly until reaching 1 for slopes above 42°. Areas with a high PoF (0.8 and above) are distributed across the entire study site (Fig. 5a) and correspond to areas with slope angles >35° (Fig. 6a). Looking at the mean PoFs, considering variations of soil thickness and root cohesion across our study site lead to a considerable decrease in PoF for slopes between 25 and 60° (Fig. 6a), with smaller values when considering the variability of all three parameters. A slight increase of the mean PoF_ST and PoF_STV are observed for slopes between 15 and 21°, which can be associated with a larger occurrence of thicker soils in this range of slope angles (Fig. 3c). The PoF_ST shows a continuous increase for slopes of 20° until reaching high values (PoF > 0.9) for slopes ranging from 45° to 55°. Then, as for the PoF, PoF_ST is equal to 1 for slopes of 60° and greater. PoF_STV shows only a continuous increase, with smaller probabilities than PoF_ST, until reaching its highest value for slopes of 60° (Fig. 6a).

Figs. 6b and c show the mean PoF_ST and PoF_STV, respectively, as function of soil thickness and slope angle. PoF_ST and PoF_STV show similar pattern with high values for slopes >30° and soil thickness > 5

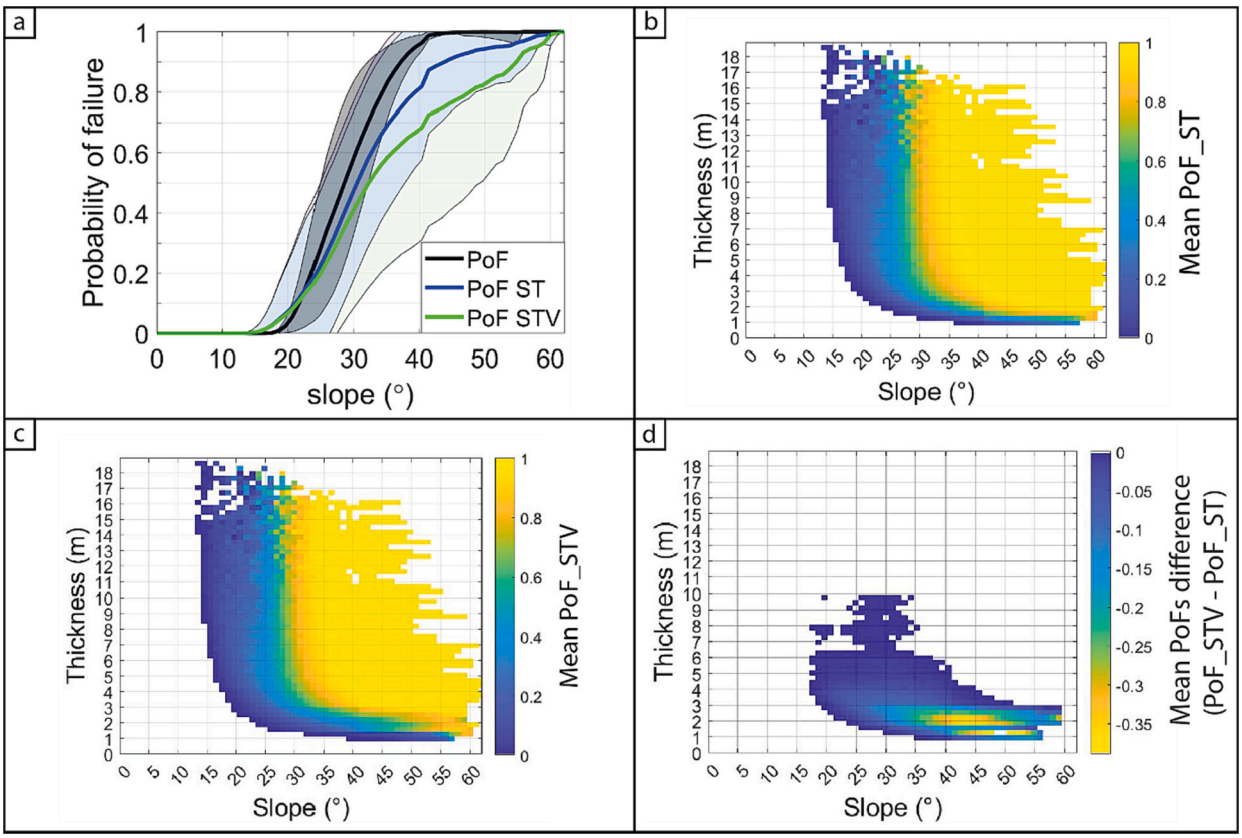

Fig. 6. a) Mean PoF (black), PoF_ST (blue) and PoF_STV (green) as a function of slope angle and the associated variability across the site expressed as standard deviation b) Mean PoF_ST as a function of slope angle and soil thickness c) Mean PoF_STV as a function of slope angle and soil thickness d) Difference of mean PoF_STV and PoF_ST as a function of slope angle and soil thickness.

m. PoF_ST and PoF_STV equal zero for slopes <15° and thickness < 0.5 m. PoF_ST shows the highest values (> 0.8) for slopes >30°, and reaches their maximum at soil thicknesses above 3 and 1 m for slopes angles above 30° and 60°, respectively. PoF_STV shows the same behavior, but for larger soil thicknesses of 5 and 1 m (Fig. 6c).

Fig. 6d shows the difference between the mean PoF_STV and PoF_ST as a function of slope and soil thickness. A general decrease of the probability is visible for slopes ranging from 17° to 60° and thicknesses between 0.5 and 10 m (Fig. 6d). However, the strongest decrease (more than −0.15) is observed for slopes ranging from 30° to 60° and soil thicknesses ranging from 1 to 3 m (Fig. 6d). Including tall vegetation in the PoF calculation leads to a considerable decrease in PoF for slope angles and soil thicknesses ranging from 37 to 50° and 1.8 to 2.5 m, respectively. The presence of tall vegetation causes a maximum reduction of PoF of −0.39 for slopes of 48° and soil thickness of 1.25 m, while it is negligible for soil thicknesses above 3 m on steep slopes (> 50°) and for soil thicknesses above 10 m for gentle slopes (15° to 35°).

4.5. PoF monitoring

During the monitoring period, eucalyptus trees were removed across a single slope of the study area to manage wildfire risk (Fig. 4, Appendix 1). To highlight the importance of accounting for the vegetation distribution, the impact of this management practice was analyzed. As outlined before, we classified the vegetation distribution for two periods, between which the tree removal took place. The first period comprised satellite images acquired on October 2020 and January 2021 during which the trees were present, while the second period included satellite images of spring/summer 2021 (April and June 2021), during which tree removal had happened already. Based on these images, vegetation was classified and PoF distributions calculated.

Fig. 7 shows the difference in the PoF after the removal of eucalyptus trees (2nd period – 1st period), and highlights the importance of accounting for the vegetation distribution, but also its time-varying nature. A considerable increase in the PoF of up to 0.8 is observed, caused by the removal of the eucalyptus trees. The PoF increased more in the western part of the area due to the thinner soils in this area (<2.5 m, Fig. 7). The eastern part, with a soil thickness of 5 m, is only slightly affected (+ 0.1). This information is very valuable in managing the changing landslide hazard, since particularly the western part of this area shows a considerable impact by the tree removal, and hence further vegetation management such as planting native coast live oak will be targeted on this area.

5. Discussion

Here, we evaluate the PoF for shallow landslides of a highly landslide-prone urban area. Through a sensitivity analysis, we show that for our study site the PoF calculation is primarily sensitive to the slope angle, the soil thickness, and the cohesion. The sensitivity analysis showed that the slope angle has the greatest influence, while soil thickness and cohesion have a similar influence on the PoF calculation. While the slope angle can be readily extracted from a high-resolution DEM, the spatial distribution of soil thickness and cohesion is more challenging to estimate. In order to retrieve spatial variations in soil thickness and root cohesion, we applied two methods that are rapid and can be reproduced easily. Analysis of ambient seismic noise recordings provide estimates of the soil thickness, and classification of satellite images allowed for a rapid and repeatable mapping of vegetation cover, which is directly related to the root network.

We analyzed the impact of the three different parameters on the PoF distribution. Only considering varying slope angles showed that slope

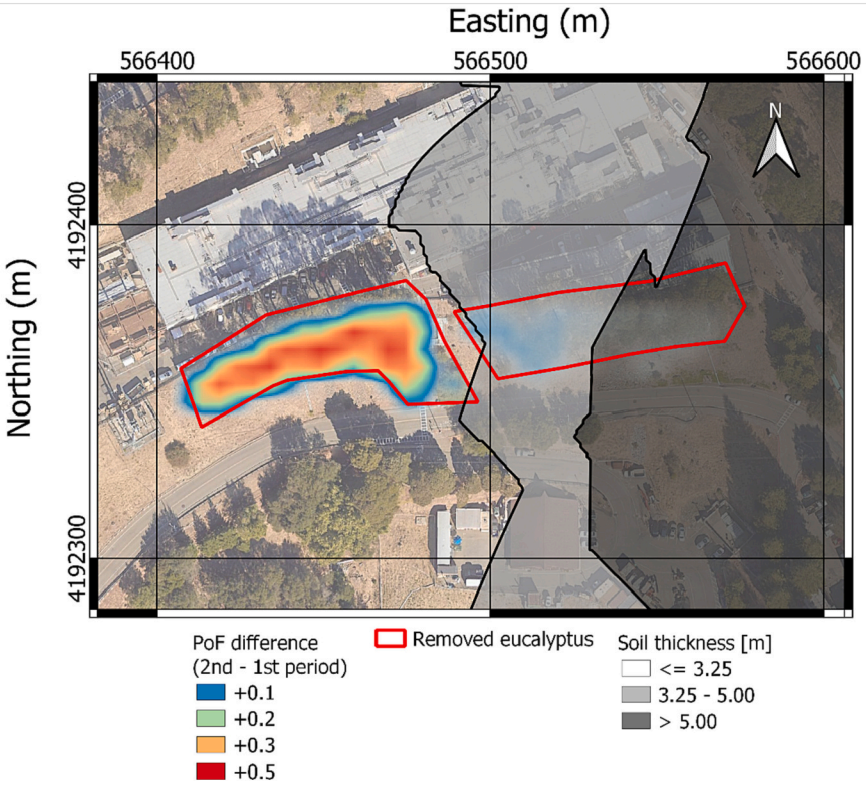

Fig. 7. PoF difference between the second and the first period, representing periods after and before removal of the eucalyptus trees. Red outlined areas highlight the managed area. Soil thickness is displayed in gray scale between 0 and 5 m.

angles increasing from 20° to 50° drastically increases the PoF until reaching a plateau close to 1. Also considering the spatial variability of soil thickness reduced the global PoF over the area from 0.26 to 0.22. Slopes steeper than 30° and with a soil thickness above 5 m are characterized by PoF of 0.9 and higher, highlighting a very high landslide hazard for these slopes. In addition, the increased amount of potential sliding mass (due to the thicker soil layers) could result in devastating impacts of landslides in these areas.

The soil cohesion was evaluated from previous geotechnical campaigns and a remote sensing approach was used to extract the vegetation cover, and hence root cohesion. We showed that root cohesion has a significant impact on slope stabilization, particularly under thin soil conditions, increasing cohesion by a factor of 12 in the first meter. Root cohesion has a beneficial impact, lowering the PoF drastically for soil thickness smaller than 3 m with slope angles between 30 and 60°, with the largest impact for soil thickness of 2 m and below. This shows that the estimated root network is not dense enough to have a significant benefit for deeper soil. In most of the cases, the root network will not reach depths larger than 7 m, with a small fraction of them going deeper than 1 m (Canadell et al., 1996) and approximately 70 % of root biomass located above 50 cm depth for woody species (Kummerow and Mangan, 1981; Jackson et al., 1996; Schulze et al., 1996). In case of larger soil thickness, vegetation could have a negative impact by adding weight to the soil, which could increase the PoF more than what can be compensated for by the increase in cohesion. However, this impact was not formally evaluated because: (i) the stem weight distribution cannot

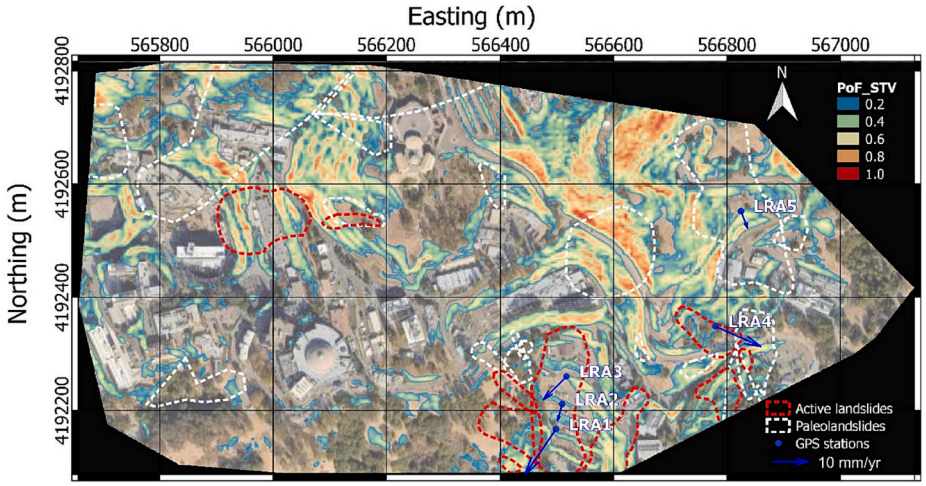

Fig. 8. Maps of active landslides and paleolandslides associated with PoF_STV and mean yearly displacement of GNSS stations.

be estimated from the satellite imagery, and (ii) the surcharge effect is often negligible compared to the soil mass itself (Fan and Lai, 2014), even more so in the case of relatively deep landslides. After integrating the spatial distribution of vegetation, the estimated PoF decreased in the south-western and north-western parts of the study area, although these are known to have experienced landslides in the past (Fig. 8). This highlights that some paleolandslides may have been mitigated by the natural or man-made addition of vegetation.

Considering the soil properties of the study area and the failure likelihood, we show that slope failure is unlikely for slopes with an angle below 20°, and that the probability of failure is increasing considerably for slopes steeper than 30°. A soil thickness of at least 1 m is required to trigger a landslide in steep slope areas (> 55°), and of at least 3 m in gentler slope areas (about 20°).

To validate our results, we analyzed average annual displacement rates, recorded by five GNSS stations (Cohen-Waeber, 2018). Each stations velocity was calculated following an approach by (Murray and Svarc, 2017), and the velocity of GNSS station P224, which is located outside the study area, was subtracted to account for tectonic plate movement. The final PoF map considering the three parameters discussed here shows that the monitored locations exhibit displacements and are located in areas of a high PoF (Fig. 8c). Indeed, all five GNSS stations showed displacements ranging from 4.8 to 15.1 mm/yr. LRA5, located in an area listed as a paleolandslide shows a displacement rate of 5 mm/yr, corresponding to a very slow-moving landslide, while LRA4, located in an active landslide domain, shows displacement rates of 15 mm/yr. Additionally, walkover surveys highlighted current landslide activity mapped with high PoF in the northwestern and central parts of the study area. This confirms the validity of the estimated PoF distribution.

The study showed that the soil thickness variability and vegetation distribution are of critical importance to the landslide risk evaluation. At the studied site, considering both distributions was necessary to assess the PoF and the risk associated with future slope failures.

Additionally, it showed that geophysical measurements, and more precisely the computation of the H/V ratio is an efficient way to extract the soil thickness at local to regional scale without requiring time-consuming and cumbersome methods. Likewise, the use of remote sensing has facilitated the extraction of vegetation landcovers and their spatial distribution, which in turn allowed us to estimate the evolution of root cohesion for the purpose of PoF monitoring. Indeed, in our case, land use management in the study area, located in the Bay Area, has led to a large number of *eucalyptus* tree removals as a measure to reduce fire hazards. Studies already implementing a real time evaluation of the landslide hazard based on a physical based model (Krøgli et al., 2018), however only considering meteorological forecast. Tree removal drastically increased the PoF in areas of thin soil (up to 3–4 m, Fig. 7). However, as shown by Schmidt et al. (2001), the added root cohesion last for few years after harvesting, depending on the tree species. The root cohesion decay after harvesting was not considered here, yet the results provide crucial information for additional vegetation management in the affected area in order to mitigate the increased landslide hazard. The same approach could also be used to monitor vegetation dynamics, and hence landslide hazards, over longer periods, by, e.g., classifying the vegetation cover 3–4 times per year. This would allow to estimate future changes in root cohesion (considering the rate of root degradation), and could contribute to monitoring landslide hazard. This would also provide a feedback pathway to adapt land management plans to include landslide hazard concerns, as outlined in the example of the eucalyptus tree removal.

The approach used in this study allowed us to consider the spatial variability of the slope angle, soil thickness, and cohesion. In addition, the sensitivity analysis showed that uncertainties in soil density, friction angle, and transmissivity have a small impact on the final PoF map. However, uncertainties in slope angle and soil thickness could have a major impact on the final PoF map. The slope angle uncertainty depends on the DEM used. In our case, the DEM used has a slope angle accuracy of about ±5°. This study highlighted that soil thickness variations have a major impact in the 0 to 5 m range, with uncertainties ranging from 0 to 1 m, respectively. The two accuracies (slope angle and soil thickness) can impact the final PoF map, however, they are small enough not to challenge the overall conclusions discussed above.

As Corominas et al. (2013) stated, it is critical to properly analyse and calibrate the parameters that are of critical importance to the hazard assessment. Without such analysis and calibration, the hazard assessment could either over- or underestimate the risk, thereby providing an unreliable estimate. Here, we addressed this issue by determining the most important parameters, and using a probabilistic approach to the hazard assessment, which accounts for variability of some of the model input parameters.

6. Conclusion/perspectives

This study shows that coupling geophysical and remote sensing data is useful to reduce uncertainty in the assessment of landslide hazards. The influence of slope angle, soil thickness, and root cohesion on estimates of slope stability were evaluated. We highlighted that for this study area slope angles above 30° have a high PoF (>0.5). Additionally, we showed that the soil thickness variability has a strong impact on the PoF of the study area. Soil thicknesses >5 m significantly increase the PoF for slope angles of 30° and greater. For thinner soil cover (1 m - 5 m), the PoF were generally low, but for very steep slopes, values of up to 1 are still possible, with higher probability at smaller angles for increasing soil thickness (i.e. 35° for 5 m, and 55° for 2 m soil thickness). The study also shows that root cohesion is only effective in slope stabilization for shallow soil thicknesses (< 3 m). The results demonstrated that the knowledge of the soil thickness distribution is essential to properly evaluate the PoF of a study area. While assuming a constant soil thickness across the area showed a high PoF throughout the study site, acknowledging variable thickness and vegetation distribution highlighted areas of an increased PoF. These areas characterized by a high PoF correlate with areas of known and currently monitored slope displacements, but also highlighted other areas of concern.

This study highlights that it is important to account for the spatial variability in soil thickness and cohesion, due to root cohesion from tall vegetation cover. To help with that, a new approach combining the use of ambient seismic noise analysis and remote sensing data was proposed, which allows for extracting these parameters easily. The analysis of ambient seismic noise records showed that we can easily extract the soil thickness in short time, while using readily available satellite imagery allows for a rapid and repeatable analysis of vegetation cover. Through assessing the impact of tree removal on the PoF, promising results for monitoring landslide hazard using remote sensing in such evolving areas have been shown. This approach could be complemented with tracking changes in soil parameters to update the PoF over time. Recent developments in wireless sensor networks and automated geophysical data acquisition allowed remote monitoring of parameters such as soil moisture and water table. Such data could be integrated into hydro-geomechanical models to provide no longer an average PoF, but a close to real-time PoF, which could provide crucial information for early warning systems. This study highlights the importance of a good understanding of the soil thickness and vegetation distribution for landslide hazard assessment, but also provides a novel and transferable methodology to account for those in the assessment of other areas at risk.

Funding

This research has been supported by the Laboratory Directed Research and Development Program of Lawrence Berkeley National Laboratory under U.S. Department of Energy Contract No. DE-AC02-05CH11231.

Declaration of competing interest

The authors declare that they have no known competing financial interests or personal relationships that could have appeared to influence the work reported in this paper.

Data availability

Data will be made available on request.

Acknowledgments

We would like to thank the NASA Commercial Smallsat Data Acquisition (CSDA) program for providing access to the Planet data used in this study.

We also acknowledge Teresa Salvatici, and two anonymous reviewers for their constructive comments that helped to improve the overall quality of the manuscript.

Appendix A

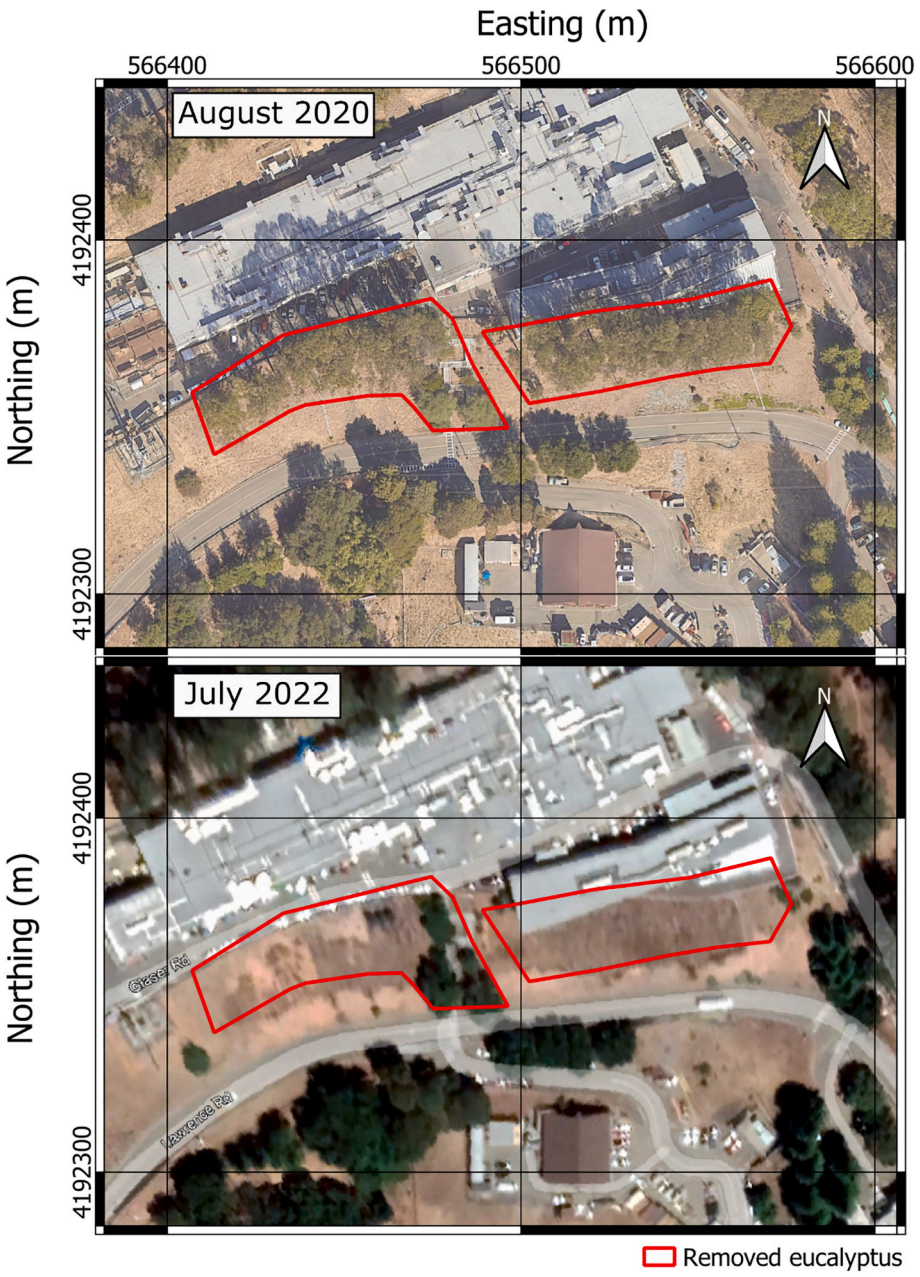

Appendix 1. Google Earth images, captured on August 6, 2020 and July 10, 2022 respectively, showing the removal of eucalyptus trees.

References

Akgun, A., 2012. A comparison of landslide susceptibility maps produced by logistic regression, multi-criteria decision, and likelihood ratio methods: a case study at İzmir, Turkey. Landslides 9, 93–106. https://doi.org/10.1007/s10346-011-0283-7.

Alan, Kropp, Associates, 2006. Initial Landslide Characterization Study East Canyon–Buildings 85 and 85A.

Aleotti, P., Chowdhury, R., 1999. Landslide hazard assessment: summary review and new perspectives. Bull. Eng. Geol. Environ. 58, 21–44. https://doi.org/10.1007/s100640050066.

Anagnostopoulos, G.G., Fatichi, S., Burlando, P., 2015. An advanced process-based distributed model for the investigation of rainfall-induced landslides: the effect of process representation and boundary conditions. Water Resour. Res. 51, 7501–7523. https://doi.org/10.1002/2015WR016909.

Band, L.E., Hwang, T., Hales, T.C., Vose, J., Ford, C., 2012. Ecosystem processes at the watershed scale: mapping and modeling ecohydrological controls of landslides. In: Geomorphology, Geospatial Technologies and Geomorphological Mapping Proceedings of the 41st Annual Binghamton Geomorphology Symposium, 137, pp. 159–167. https://doi.org/10.1016/j.geomorph.2011.06.025.

Baum, L., Savage, W.Z., Godt, J.W., 2008. TRIGRS-A Fortran program for transient rainfall infiltration and grid-based regional slope-stability analysis, version 2.0. available at. In: US Geological Survey Open-File Report 2008–1159. http://pubs.usgs.gov/of/2008/1159.

Bièvre, G., Knieß, U., Jongmans, D., Pathier, E., Schwartz, S., van Westen, C.J., Villemin, T., Zumbo, V., 2011. Paleotopographic control of landslides in lacustrine deposits (Trièves plateau, French Western Alps). Geomorphology 125, 214–224. https://doi.org/10.1016/j.geomorph.2010.09.018.

Canadell, J., Jackson, R.B., Ehleringer, J.B., Mooney, H.A., Sala, O.E., Schulze, E.-D., 1996. Maximum rooting depth of vegetation types at the global scale. Oecologia 108, 583–595. https://doi.org/10.1007/BF00329030.

Cervi, F., Berti, M., Borgatti, L., Ronchetti, F., Manenti, F., Corsini, A., 2010. Comparing predictive capability of statistical and deterministic methods for landslide susceptibility mapping: a case study in the northern Apennines (Reggio Emilia Province, Italy). Landslides 7, 433–444. https://doi.org/10.1007/s10346-010-0207-y.

Chen, T., Niu, R., Jia, X., 2016. A comparison of information value and logistic regression models in landslide susceptibility mapping by using GIS. Environ. Earth Sci. 75, 867. https://doi.org/10.1007/s12665-016-5317-y.

Chen, T., Trinder, J.C., Niu, R., 2017. Object-oriented landslide mapping using ZY-3 satellite imagery, random forest and mathematical morphology, for the Three-Gorges Reservoir, China. Remote Sens. 9, 333. https://doi.org/10.3390/rs9040333.

Chen, W., Peng, J., Hong, H., Shahabi, H., Pradhan, B., Liu, J., Zhu, A.-X., Pei, X., Duan, Z., 2018. Landslide susceptibility modelling using GIS-based machine learning techniques for Chongren County, Jiangxi Province, China. Sci. Total Environ. 626, 1121–1135. https://doi.org/10.1016/j.scitotenv.2018.01.124.

Cheung, R.W.M., 2021. Landslide risk management in Hong Kong. Landslides 18, 3457–3473. https://doi.org/10.1007/s10346-020-01587-0.

Choo, H., Min, D.-H., Sung, J.H., Yoon, H.-K., 2019. Sensitivities of input parameters for predicting stability of soil slope. Bull. Eng. Geol. Environ. 78, 5671–5685. https://doi.org/10.1007/s10064-019-01503-4.

Coe, J.A., 2020. Bellwether sites for evaluating changes in landslide frequency and magnitude in cryospheric mountainous terrain: a call for systematic, long-term observations to decipher the impact of climate change. Landslides 17, 2483–2501. https://doi.org/10.1007/s10346-020-01462-y.

Cohen, D., Schwarz, M., 2017. Tree-root control of shallow landslides. Earth Surf. Dyn. 5, 451–477. https://doi.org/10.5194/esurf-5-451-2017.

Cohen-Waeber, J.F., 2018. Spatiotemporal Patterns of Seasonality in Landslide Deformation from InSAR and GPS (Ph.D.). University of California, Berkeley, United States – California.

A3GEO, Inc, 2020. Geotechnical Data and Interpretations Report Fiscal Year 2020 Ground Motions Study Lawrence Berkeley National Laboratory Berkeley, California.

QGIS, D.T, 2020. QGIS Geographic Information System.

Quantum Spatial, I., 2019. Northern California 3DEP QL1 QL2 LiDAR Project Report.

Corominas, J., van Westen, C., Frattini, P., Cascini, L., Malet, J.-P., Fotopoulou, S., Catani, F., Van Den Eeckhaut, M., Mavrouli, O., Agliardi, F., Pitilakis, K., Winter, M. G., Pastor, M., Ferlisi, S., Tofani, V., Hervás, J., Smith, J.T., 2013. Recommendations for the quantitative analysis of landslide risk. Bull. Eng. Geol. Environ. https://doi.org/10.1007/s10064-013-0538-8.

De Graff, J.V., 2018. A rationale for effective post-fire debris flow mitigation within forested terrain. Geoenviron. Disasters 5, 7. https://doi.org/10.1186/s40677-018-0099-z.

Devkota, K.C., Regmi, A.D., Pourghasemi, H.R., Yoshida, K., Pradhan, B., Ryu, I.C., Dhital, M.R., Althuwaynee, O.F., 2013. Landslide susceptibility mapping using certainty factor, index of entropy and logistic regression models in GIS and their comparison at Mugling-Narayanghat road section in Nepal Himalaya. Nat. Hazards 65, 135–165. https://doi.org/10.1007/s11069-012-0347-6.

Di Napoli, M., Di Martire, D., Bausilio, G., Calcaterra, D., Confuorto, P., Firpo, M., Pepe, G., Cevasco, A., 2021. Rainfall-induced shallow landslide detachment, transit and runout susceptibility mapping by integrating machine learning techniques and GIS-based approaches. Water 13, 488. https://doi.org/10.3390/w13040488.

Emadi-Tafti, M., Ataie-Ashtiani, B., Hosseini, S.M., 2021. Integrated impacts of vegetation and soil type on slope stability: a case study of Kheyrud Forest, Iran. Ecol. Model. 446, 109498 https://doi.org/10.1016/j.ecolmodel.2021.109498.

Erinjery, J.J., Singh, M., Kent, R., 2018. Mapping and assessment of vegetation types in the tropical rainforests of the Western Ghats using multispectral Sentinel-2 and SAR Sentinel-1 satellite imagery. Remote Sens. Environ. 216, 345–354. https://doi.org/10.1016/j.rse.2018.07.006.

Falco, N., Xia, J., Kang, X., Li, S., Benediktsson, J.A., 2020. Chapter 2.10 - Supervised classification methods in hyperspectral imaging—recent advances. In: Amigo, J.M. (Ed.), Data Handling in Science and Technology, Hyperspectral Imaging. Elsevier, pp. 247–279. https://doi.org/10.1016/B978-0-444-63977-6.00012-2.

Falco, N., Wainwright, H.M., Dafflon, B., Ulrich, C., Soom, F., Peterson, J.E., Brown, J.B., Schaettle, K.B., Williamson, M., Cothren, J.D., Ham, R.G., McEntire, J.A., Hubbard, S.S., 2021. Influence of soil heterogeneity on soybean plant development and crop yield evaluated using time-series of UAV and ground-based geophysical imagery. Sci. Rep. 11, 7046. https://doi.org/10.1038/s41598-021-86480-z.

Fan, C.-C., Lai, Y.-F., 2014. Influence of the spatial layout of vegetation on the stability of slopes. Plant Soil 377, 83–95. https://doi.org/10.1007/s11104-012-1569-9.

Field, E.H., 2008. The uniform California earthquake rupture forecast, version 2 (UCERF 2). In: US Geological Survey.

Forbes, K., Broadhead, J., 2013. Forests and Landslides: The Role of Trees and Forests in the Prevention of Landslides and Rehabilitation of Landslide-affected Areas in Asia. Food and Agriculture Organization of the United Nations, Bangkok.

Froude, M.J., Petley, D., 2018. Global fatal landslide occurrence from 2004 to 2016. Nat. Hazards Earth Syst. Sci. 18, 2161–2181.

Gehring, E., Conedera, M., Maringer, J., Giadrossich, F., Guastini, E., Schwarz, M., 2019. Shallow landslide disposition in burnt european beech (Fagus sylvatica L.) forests. Sci. Rep. 9, 8638. https://doi.org/10.1038/s41598-019-45073-7.

Gorsevski, P.V., Brown, M.K., Panter, K., Onasch, C.M., Simic, A., Snyder, J., 2016. Landslide detection and susceptibility mapping using LiDAR and an artificial neural network approach: a case study in the Cuyahoga Valley National Park, Ohio. Landslides 13, 467–484. https://doi.org/10.1007/s10346-015-0587-0.

Guéguen, P., Cornou, C., Garambois, S., Banton, J., 2007. On the limitation of the H/V spectral ratio using seismic noise as an exploration tool: application to the Grenoble Valley (France), a Small Apex Ratio Basin. Pure Appl. Geophys. 164, 115–134. https://doi.org/10.1007/s00024-006-0151-x.

Guzzetti, F., Carrara, A., Cardinali, M., Reichenbach, P., 1999. Landslide hazard evaluation: a review of current techniques and their application in a multi-scale study, Central Italy. Geomorphology 31, 181–216. https://doi.org/10.1016/S0169-555X(99)00078-1.

Hammond, C.J., Prellwitz, R.W., Miller, S.M., 1992. Landslide hazard assessment using Monte Carlo simulation. In: Proceedings of 6th International Symposium on Landslides, Christchurch, New Zealand, Balkema, pp. 251–294.

Haque, U., da Silva, P.F., Devoli, G., Pilz, J., Zhao, B., Khaloua, A., Wilopo, W., Andersen, P., Lu, P., Lee, J., Yamamoto, T., Keellings, D., Wu, J.-H., Glass, G.E., 2019. The human cost of global warming: deadly landslides and their triggers (1995–2014). Sci. Total Environ. 682, 673–684. https://doi.org/10.1016/j.scitotenv.2019.03.415.

Hobley, D.E.J., Adams, J.M., Nudurupati, S.S., Hutton, E.W.H., Gasparini, N.M., Istanbulluoglu, E., Tucker, G.E., 2017. Creative computing with Landlab: an open-source toolkit for building, coupling, and exploring two-dimensional numerical models of Earth-surface dynamics. Earth Surf. Dyn. 5, 21–46. https://doi.org/10.5194/esurf-5-21-2017.

Hungr, O., Leroueil, S., Picarelli, L., 2014. The Varnes classification of landslide types, an update. Landslides 11, 167–194. https://doi.org/10.1007/s10346-013-0436-y.

Hwang, T., Band, L.E., Hales, T.C., Miniat, C.F., Vose, J.M., Bolstad, P.V., Miles, B., Price, K., 2015. Simulating vegetation controls on hurricane-induced shallow landslides with a distributed ecohydrological model. J. Geophys. Res. Biogeosci. 120, 361–378. https://doi.org/10.1002/2014JG002824.

Jackson, M., Roering, J.J., 2009. Post-fire geomorphic response in steep, forested landscapes: Oregon Coast Range, USA. Quat. Sci. Rev. 28, 1131–1146. https://doi.org/10.1016/j.quascirev.2008.05.003.

Jackson, R.B., Canadell, J., Ehleringer, J.R., Mooney, H.A., Sala, O.E., Schulze, E.D., 1996. A global analysis of root distributions for terrestrial biomes. Oecologia 108, 389–411. https://doi.org/10.1007/BF00333714.

Ji, J., Kokutse, N., Genet, M., Fourcaud, T., Zhang, Z., 2012. Effect of spatial variation of tree root characteristics on slope stability. a case study on Black Locust (Robinia pseudoacacia) and Arborvitae (Platycladus orientalis) stands on the Loess Plateau, China. CATENA 92, 139–154. https://doi.org/10.1016/j.catena.2011.12.008.

Ji, J., Mao, Z., Qu, W., Zhang, Z., 2020. Energy-based fibre bundle model algorithms to predict soil reinforcement by roots. Plant Soil 446, 307–329. https://doi.org/10.1007/s11104-019-04327-z.

Jones, D.L., Curtis, G.H., 1991. Guide to the geology of the Berkeley Hills, central Coast Ranges, California. In: Geol. Excursions North. Calif. San Franc. Sierra Nev. Calif. Div. Mines Geol. Spec. Publ, 109, pp. 63–74.

Jovančević, S.D., Nagai, O., Sassa, K., Arbanas, Ž., 2013. In: Deterministic Landslide Susceptibility Analyses Using LS-Rapid Software, pp. 73–77.

Kalantar, B., Ueda, N., Saeidi, V., Ahmadi, K., Halin, A.A., Shabani, F., 2020. Landslide susceptibility mapping: machine and ensemble learning based on remote sensing big data. Remote Sens. 12, 1737. https://doi.org/10.3390/rs12111737.

Kim, J.H., Fourcaud, T., Jourdan, C., Maeght, J.-L., Mao, Z., Metayer, J., Meylan, L., Pierret, A., Rapidel, B., Roupsard, O., de Rouw, A., Sanchez, M.V., Wang, Y., Stokes, A., 2017. Vegetation as a driver of temporal variations in slope stability: the impact of hydrological processes. Geophys. Res. Lett. 44, 4897–4907. https://doi.org/10.1002/2017GL073174.

Konno, K., Ohmachi, T., 1998. Ground-motion characteristics estimated from spectral ratio between horizontal and vertical components of microtremor. Bull. Seismol. Soc. Am. 88, 228–241. https://doi.org/10.1785/BSSA0880010228.

Kramer, S.L., 1996. Earthquake Geotechnical Engineering. Prentice Hall, Upper Saddle River, NJ.

Krøgli, I.K., Devoli, G., Colleuille, H., Boje, S., Sund, M., Engen, I.K., 2018. The norwegian forecasting and warning service for rainfall- and snowmelt-induced landslides. Nat. Hazards Earth Syst. Sci. 18, 1427–1450. https://doi.org/10.5194/nhess-18-1427-2018.

Kummerow, J., Mangan, R., 1981. Root systems in Quercus dumosa Nutt. dominated chaparral in southern California. Acta Oecol. 2, 177–188.

Kuriakose, S.L., van Beek, L.P.H., 2011. Plant root strength and slope stability. In: Gliński, J., Horabik, J., Lipiec, J. (Eds.), Encyclopedia of Agrophysics. Springer Netherlands, Dordrecht, pp. 622–627. https://doi.org/10.1007/978-90-481-3585-1_222.

Lanini, J.S., Clark, E.A., Lettenmaier, D.P., 2009. Effects of fire-precipitation timing and regime on post-fire sediment delivery in Pacific Northwest forests. Geophys. Res. Lett. 36 https://doi.org/10.1029/2008GL034588.

Le Roux, O., Schwartz, S., Gamond, J.F., Jongmans, D., Tricart, P., Sebrier, M., 2010. Interaction between tectonic and erosion processes on the morphogenesis of an Alpine valley: geological and geophysical investigations in the lower Romanche valley (Belledonne massif, western Alps). Int. J. Earth Sci. 99, 427–441. https://doi.org/10.1007/s00531-008-0393-1.

Lee, S., Jang, J., Kim, Y., Cho, N., Lee, M.-J., 2020. Susceptibility analysis of the Mt. Umyeon landslide area using a physical slope model and probabilistic method. Remote Sens. 12, 2663. https://doi.org/10.3390/rs12162663.

Li, S.H., Luo, X.H., Wu, L.Z., 2021. A new method for calculating failure probability of landslide based on ANN and a convex set model. Landslides 18, 2855–2867. https://doi.org/10.1007/s10346-021-01652-2.

Lin, Q., Wang, Y., Glade, T., Zhang, J., Zhang, Y., 2020. Assessing the spatiotemporal impact of climate change on event rainfall characteristics influencing landslide occurrences based on multiple GCM projections in China. Clim. Chang. 162, 761–779. https://doi.org/10.1007/s10584-020-02750-1.

Liu, Y., Gong, W., Hu, X., Gong, J., 2018. Forest type identification with Random Forest using Sentinel-1A, Sentinel-2A, Multi-temporal Landsat-8 and DEM data. Remote Sens. 10, 946. https://doi.org/10.3390/rs10060946.

Liu, H., Mao, Z., Wang, Y., Kim, J.H., Bourrier, F., Mohamed, A., Stokes, A., 2021. Slow recovery from soil disturbance increases susceptibility of high elevation forests to landslides. For. Ecol. Manag. 485, 118891 https://doi.org/10.1016/j.foreco.2020.118891.

Mao, Z., Yang, M., Bourrier, F., Fourcaud, T., 2014. Evaluation of root reinforcement models using numerical modelling approaches. Plant Soil 381, 249–270. https://doi.org/10.1007/s11104-014-2116-7.

Marelli, S., Sudret, B., 2014. In: UQLab: A Framework for Uncertainty Quantification in Matlab, pp. 2554–2563. https://doi.org/10.1061/9780784413609.257.

Marjanović, M., Kovačević, M., Bajat, B., Voženílek, V., 2011. Landslide susceptibility assessment using SVM machine learning algorithm. Eng. Geol. 123, 225–234. https://doi.org/10.1016/j.enggeo.2011.09.006.

Mattia, C., Bischetti, G.B., Gentile, F., 2005. Biotechnical characteristics of root systems of typical Mediterranean Species. Plant Soil 278, 23–32. https://doi.org/10.1007/s11104-005-7930-5.

Méric, O., Garambois, S., Malet, J.-P., Cadet, H., Guéguen, P., Jongmans, D., 2007. Seismic noise-based methods for soft-rock landslide characterization. Bull. Soc. Geol. Fr. 178, 137. https://doi.org/10.2113/gssgfbull.178.2.137.

Min, D.-H., Yoon, H.-K., 2021. Suggestion for a new deterministic model coupled with machine learning techniques for landslide susceptibility mapping. Sci. Rep. 11, 6594. https://doi.org/10.1038/s41598-021-86137-x.

Montrasio, L., Valentino, R., Losi, G.L., 2011. Towards a real-time susceptibility assessment of rainfall-induced shallow landslides on a regional scale. Nat. Hazards Earth Syst. Sci. 11, 1927–1947. https://doi.org/10.5194/nhess-11-1927-2011.

Mountrakis, G., Im, J., Ogole, C., 2011. Support vector machines in remote sensing: a review. ISPRS J. Photogramm. Remote Sens. 66, 247–259. https://doi.org/10.1016/j.isprsjprs.2010.11.001.

Murray, J.R., Svarc, J., 2017. Global positioning system data collection, processing, and analysis conducted by the U.S. Geological Survey earthquake hazards program. Seismol. Res. Lett. 88, 916–925. https://doi.org/10.1785/0220160204.

Nilsen, B., 2000. New trends in rock slope stability analyses. Bull. Eng. Geol. Environ. 58, 173–178. https://doi.org/10.1007/s100640050072.

Norris, J.E., 2005. Root reinforcement by Hawthorn and Oak Roots on a Highway Cut-Slope in Southern England. Plant Soil 278, 43–53. https://doi.org/10.1007/s11104-005-1301-0.

Nourani, V., Pradhan, B., Ghaffari, H., Sharifi, S.S., 2014. Landslide susceptibility mapping at Zonouz Plain, Iran using genetic programming and comparison with frequency ratio, logistic regression, and artificial neural network models. Nat. Hazards 71, 523–547. https://doi.org/10.1007/s11069-013-0932-3.

Palazzolo, N., Peres, D.J., Bordoni, M., Meisina, C., Creaco, E., Cancelliere, A., 2021. Improving spatial landslide prediction with 3D slope stability analysis and genetic algorithm optimization: application to the Oltrepò Pavese. Water 13, 801. https://doi.org/10.3390/w13060801.

Park, S., Choi, C., Kim, B., Kim, J., 2013. Landslide susceptibility mapping using frequency ratio, analytic hierarchy process, logistic regression, and artificial neural network methods at the Inje area, Korea. Environ. Earth Sci. 68, 1443–1464. https://doi.org/10.1007/s12665-012-1842-5.

Patton, A.I., Rathburn, S.L., Capps, D.M., 2019. Landslide response to climate change in permafrost regions. Geomorphology 340, 116–128. https://doi.org/10.1016/j.geomorph.2019.04.029.

Pedregosa, F., Varoquaux, G., Gramfort, A., Michel, V., Thirion, B., Grisel, O., Blondel, M., Prettenhofer, P., Weiss, R., Dubourg, V., Vanderplas, J., Passos, A., Cournapeau, D., Brucher, M., Perrot, M., Duchesnay, É., 2011. Scikit-learn: machine learning in Python. J. Mach. Learn. Res. 12, 2825–2830.

Phillips, C., Hales, T., Smith, H., Basher, L., 2021. Shallow landslides and vegetation at the catchment scale: a perspective. Ecol. Eng. 173, 106436 https://doi.org/10.1016/j.ecoleng.2021.106436.

Preti, F., 2006. On root reinforcement modeling. European Geosciences Union 2006. In: Geophysical Research Abstracts, p. 04555.

Regmi, A.D., Devkota, K.C., Yoshida, K., Pradhan, B., Pourghasemi, H.R., Kumamoto, T., Akgun, A., 2014. Application of frequency ratio, statistical index, and weights-of-evidence models and their comparison in landslide susceptibility mapping in Central Nepal Himalaya. Arab. J. Geosci. 7, 725–742. https://doi.org/10.1007/s12517-012-0807-z.

Reichenbach, P., Rossi, M., Malamud, B.D., Mihir, M., Guzzetti, F., 2018. A review of statistically-based landslide susceptibility models. Earth-Sci. Rev. 180, 60–91. https://doi.org/10.1016/j.earscirev.2018.03.001.

Rengers, F.K., McGuire, L.A., Oakley, N.S., Kean, J.W., Staley, D.M., Tang, H., 2020. Landslides after wildfire: initiation, magnitude, and mobility. Landslides 17, 2631–2641. https://doi.org/10.1007/s10346-020-01506-3.

Schmidt, K.M., Roering, J.J., Stock, J.D., Dietrich, W.E., Montgomery, D.R., Schaub, T., 2001. The variability of root cohesion as an influence on shallow landslide susceptibility in the Oregon Coast Range. Can. Geotech. J. 38, 995–1024. https://doi.org/10.1139/t01-031.

Schulze, E.-D., Mooney, H.A., Sala, O.E., Jobbagy, E., Buchmann, N., Bauer, G., Canadell, J., Jackson, R.B., Loreti, J., Oesterheld, M., Ehleringer, J.R., 1996. Rooting depth, water availability, and vegetation cover along an aridity gradient in Patagonia. Oecologia 108, 503–511. https://doi.org/10.1007/BF00333727.

Segoni, S., Rossi, G., Catani, F., 2012. Improving basin scale shallow landslide modelling using reliable soil thickness maps. Nat. Hazards 61, 85–101. https://doi.org/10.1007/s11069-011-9770-3.

SESAME, 2004. In: Guidelines for the Implementation of the H/V Spectral Ratio Technique on Ambient Vibrations: Measurements, Processing and Interpretation, SESAME European Research Project, WP12—Deliverable D23, 12. EVG1-CT-2000-00026, pp. 1–62.

Sidle, R.C., Bogaard, T.A., 2016. Dynamic earth system and ecological controls of rainfall-initiated landslides. Earth-Sci. Rev. 159, 275–291. https://doi.org/10.1016/j.earscirev.2016.05.013.

Sidle, R.C., Ochiai, H., 2006. Landslides: Processes, Prediction and Land Use, Water Resources Monograph. American Geophysical Union, Washington, DC.

Sobol′, I.M., 2001. Global sensitivity indices for nonlinear mathematical models and their Monte Carlo estimates. In: Math. Comput. Simul., The Second IMACS Seminar on Monte Carlo Methods, 55, pp. 271–280. https://doi.org/10.1016/S0378-4754(00)00270-6.

Strauch, R., Istanbulluoglu, E., Nudurupati, S.S., Bandaragoda, C., Gasparini, N.M., Tucker, G.E., 2018. A hydroclimatological approach to predicting regional landslide probability using Landlab. Earth Surf. Dyn. 6, 49–75. https://doi.org/10.5194/esurf-6-49-2018.

Strauch, R., Istanbulluoglu, E., Riedel, J., 2019. A new approach to mapping landslide hazards: a probabilistic integration of empirical and physically based models in the North Cascades of Washington, USA. Nat. Hazards Earth Syst. Sci. 19, 2477–2495. https://doi.org/10.5194/nhess-19-2477-2019.

Sudmeyer, R.A., Speijers, J., Nicholas, B.D., 2004. Root distribution of Pinus pinaster, P. Radiata, Eucalyptus globulus and E. Kochii and associated soil chemistry in agricultural land adjacent to tree lines †. Tree Physiol. 24, 1333–1346. https://doi.org/10.1093/treephys/24.12.1333.

Tien Bui, D., Tuan, T.A., Klempe, H., Pradhan, B., Revhaug, I., 2016. Spatial prediction models for shallow landslide hazards: a comparative assessment of the efficacy of support vector machines, artificial neural networks, kernel logistic regression, and logistic model tree. Landslides 13, 361–378. https://doi.org/10.1007/s10346-015-0557-6.

Tsangaratos, P., Benardos, A., 2014. Estimating landslide susceptibility through a artificial neural network classifier. Nat. Hazards 74, 1489–1516. https://doi.org/10.1007/s11069-014-1245-x.

Uhlemann, S., Chambers, J., Meldrum, P., McClure, P., Dafflon, B., 2021. Geophysical monitoring of landslides–a step closer towards predictive understanding? In: Casagli, N., Tofani, V., Sassa, K., Bobrowsky, P.T., Takara, K. (Eds.), Understanding and Reducing Landslide Disaster Risk: Volume 3 Monitoring and Early Warning, ICL Contribution to Landslide Disaster Risk Reduction. Springer International Publishing, Cham, pp. 85–91. https://doi.org/10.1007/978-3-030-60311-3_8.

Wahrhaftig, C., Sloan, D., 1989. Geology of San Francisco and vicinity. Am. Geophys. Union. Guidebook T105,, 69.

Waldron, L.J., 1977. The shear resistance of root-permeated homogeneous and stratified soil. Soil Sci. Soc. Am. J. 41, 843–849. https://doi.org/10.2136/sssaj1977.03615995004100050005x.

Wathelet, M., Jongmans, D., Ohrnberger, M., 2004. Surface-wave inversion using a direct search algorithm and its application to ambient vibration measurements. Surf. Geophys. 2, 211–221. https://doi.org/10.3997/1873-0604.2004018.

van Westen, C.J., van Asch, T.W.J., Soeters, R., 2006. Landslide hazard and risk zonation—why is it still so difficult? Bull. Eng. Geol. Environ. 65, 167–184. https://doi.org/10.1007/s10064-005-0023-0.

Wu, T.H., McKinnell III, W.P., Swanston III, D.N., 1979. Strength of tree roots and landslides on Prince of Wales Island, Alaska. Can. Geotech. J. 16, 19–33. https://doi.org/10.1139/t79-003.

Yilmaz, I., 2010a. The effect of the sampling strategies on the landslide susceptibility mapping by conditional probability and artificial neural networks. Environ. Earth Sci. 60, 505–519. https://doi.org/10.1007/s12665-009-0191-5.

Yilmaz, I., 2010b. Comparison of landslide susceptibility mapping methodologies for Koyulhisar, Turkey: conditional probability, logistic regression, artificial neural

networks, and support vector machine. Environ. Earth Sci. 61, 821–836. https://doi.org/10.1007/s12665-009-0394-9.

Yılmaz, S., Dinç, S., Alpaslan, N., 2021. Measuring the sediment thickness in urban areas using H/V spectral ratio method in Batman region, Southeast Turkey. Arab. J. Geosci. 14, 230. https://doi.org/10.1007/s12517-021-06455-2.

Youssef, A.M., Pourghasemi, H.R., Pourtaghi, Z.S., Al-Katheeri, M.M., 2016. Landslide susceptibility mapping using random forest, boosted regression tree, classification and regression tree, and general linear models and comparison of their performance at Wadi Tayyah Basin, Asir Region, Saudi Arabia. Landslides 13, 839–856. https://doi.org/10.1007/s10346-015-0614-1.

Zizioli, D., Meisina, C., Valentino, R., Montrasio, L., 2013. Comparison between different approaches to modeling shallow landslide susceptibility: a case history in Oltrepo Pavese, Northern Italy. Nat. Hazards Earth Syst. Sci. 13, 559–573. https://doi.org/10.5194/nhess-13-559-2013.